AIAA 2004-3676

Hot Flow Model of the Vortex Cold Wall Liquid Rocket

D. Fang and J. Majdalani
Advanced Theoretical Research Center
University of Tennessee Space Institute
Tullahoma, TN 37388

M. J. Chiaverini
Space Center
Orbital Technologies Corporation (ORBITEC)
Madison, WI 53717

40th AIAA/ASME/SAE/ASEE Joint Propulsion Conference and Exhibit
11–14 July 2004
Fort Lauderdale, FL

40th AIAA/ASME/SAE/ASEE Joint Propulsion Conference and Exhibit
11-14 July 2004, Fort Lauderdale, Florida

AIAA 2004-3676

Hot Flow Model of the Vortex Cold Wall Liquid Rocket

Dianqi Fang* and Joseph Majdalani†
University of Tennessee Space Institute, Tullahoma, TN 37388
and
Martin J. Chiaverini‡
Orbital Technologies Corporation, Madison, WI 53717

This study details the reactive flow simulation of the NASA sponsored cold wall bidirectional vortex chamber (CWBVC). The main features of the CWBVC are discussed in a former article in which the flow was treated as incompressible (see Fang, D., Majdalani, J., and Chiaverini, M. J., "Simulation of the Cold Wall Swirl Driven Combustion Chamber," AIAA Paper 2003-5055, July 2003). The current reactive flow model is based on a two-stage, choked nozzle approach. Knowing that the nozzle is choked at the throat under normal operation, the CWBVC chamber is decomposed into two parts: the first part extends from the head end to the nozzle throat while the second extends from the throat to the nozzle exit plane. In the first simulation stage, the incompressible flow model is applied with the divergent part of the nozzle truncated out. In the second stage, compressibility is superimposed starting with the output from Stage I. This two-stage simulation reduces CPU time and helps to achieve convergence of the compressible, reactive flow model. Our simulations rely on a commercial CFD solver to handle the steady-state, three-dimensional, Navier-Stokes equations. Specifically, we employ a 3D, segregated, implicit, absolute scheme in conjunction with the realizable $\kappa - \varepsilon$ turbulence model of Launder and Spalding. Reaction mechanisms are simulated using the non-premixed combustion model with the adiabatic PDF look-up tables. The eight conventional chemical species are used in simulating hydrogen-oxygen combustion; these include: O_2, H_2, H_2O, HO_2, H_2O_2, O, H and OH. At the conclusion of the reactive flow simulation, the existence of a bidirectional flow is demonstrated and the spatial invariance of the so-called mantle (that separates inner and outer vortex regions) is discussed. The cold wall effect is clearly extrapolated from the temperature maps over the combustion chamber wall. At the nozzle exit, shock waves are detected due to over-expansion.

I. Introduction

TURBULENT combustion is often encountered in propulsive and energy conversion systems such as chemical rockets,[1] IC engines, gas turbines, industrial burners, and commercial furnaces. Considering the limitations of analytical techniques in simulating the complex physical processes that accompany turbulent combustion, direct reliance on commercial CFD software is becoming more and more customary. By way of example, one may enumerate a plethora of dedicated packages such as FLUENT, FIRE, KIVA, VULCAN, WIND, STAR-CD, CFX, CFDRC-ACE, FLOW-3D, and others. In the absence of a single infallible program, most codes in use today appear to be undergoing an evolutionary process through which incremental improvements are constantly incorporated for the purpose of meeting the ever rising challenges of thermofluid modeling. The current study constitutes one such example in which FLUENT is chosen to model the compressible and reactive field inside a bidirectional vortex engine. Referred to as CWBVC (Cold Wall Bidirectional Vortex Chamber), the main features of this engine are described by Fang, Majdalani and Chiaverini.[1] In essence, the internal CWBVC field comprises an inner (core, reactive) vortex region surrounded by an outer (annular, non-reactive) vortex separating the combusting gases from the wall.[2] Since the outer vortex is chiefly composed of gaseous oxidizer, it provides a cool thermal blanket that protects the wall by preventing contact with the combustion products which, by design, remain confined to the core region.

*Graduate Research Associate, Marquette University, Department of Mechanical and Industrial Engineering. Member AIAA.

†Jack D. Whitfield Professor of High Speed Flows, Department of Mechanical, Aerospace and Biomedical Engineering. Member AIAA.

‡Lead Propulsion Engineer. Member AIAA.

The complex motion attributed to the bidirectional vortex exhibits three-dimensionality, turbulence, and complex interactive effects of chemical combustion processes and heat transfer. The main purpose of the current investigation is to simulate the compressible CWBVC flowfield and use the results to corroborate experimental[3] and theoretical studies[4-6] carried out concurrently. This work constitutes an extension to the previous CWBVC simulation in which the flow was treated as incompressible.[1]

The CFD program[7] provides several models for handling reacting flows. These include 1) the generalized finite-rate model, 2) the non-premixed combustion model, 3) the premixed combustion model, 4) the partially premixed combustion model, and 5) the composition PDF transport model. To simulate the CWBVC combustion field, the second, namely, the non-premixed combustion model, is adopted here. Considering the small relative proportion of heat loss from the chamber, we assume no heat transfer to the surroundings; the resulting adiabatic non-premixed combustion model requires the building of an adiabatic Probability Density Function (PDF) table using the 'prePDF' module.[7] This information is then transferred from the PDF table into the CFD solver.

For the purpose of expediting the compressible flow simulation, a two-stage choked nozzle approach is used. A schematic of the two-stage choked nozzle model is provided in Fig. 1. Knowing that the nozzle is choked at the throat, the CWBVC chamber is decomposed into two parts: one part extends from the head end to the nozzle throat (shown in Fig. 1a); the second part (Fig. 1b) continues from the nozzle throat to the nozzle exit plane. At first, the incompressible flow model is applied (with the divergent nozzle part truncated out). Once convergence of the incompressible Stage I solution is realized, compressibility is superimposed with the addition of the nozzle. This two stage simulation reduces CPU time and helps to precipitate convergence.

II. Choked Nozzle Stage I Simulation

A. Domain Size and Mesh Parameters

Figure 2 illustrates the geometry used at the beginning of the reactive flow simulation. The surface boundary shows nine velocity-inlets (four radial inlets with 0.51 inch radii near the top for gaseous hydrogen (GH_2) injection, four tangential inlets with 0.555 inch radii near the bottom for gaseous oxygen (GO_2) injection, and one axial inlet with a 0.555 inch radius at the top for secondary GO_2 injection); the chamber is truncated at the bottom with a single outflow bearing a 0.25 inch outlet radius at the throat section. The chamber is 2 inches in length and 2 inches in diameter.

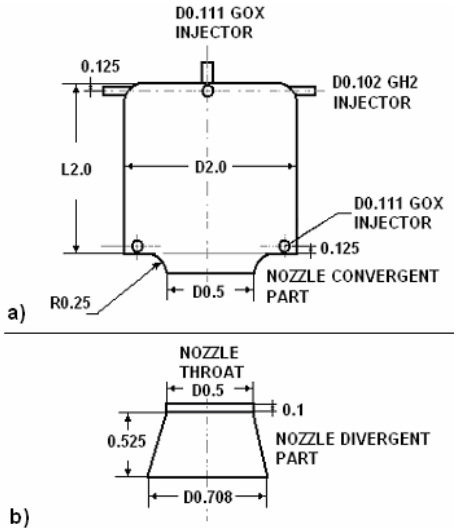

Fig. 1 Two-stage composite model consisting of a) main combustion chamber part, and b) nozzle part.

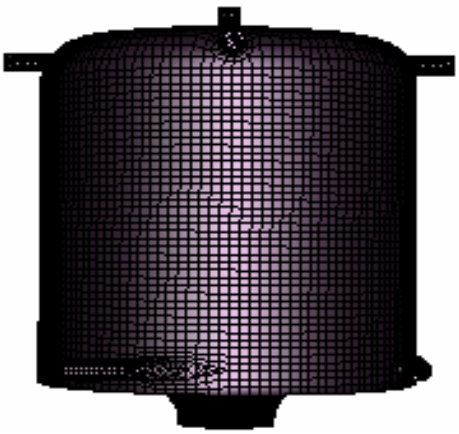

Fig. 2 Surface boundary (with grid display) for the Stage I incompressible flow simulation.

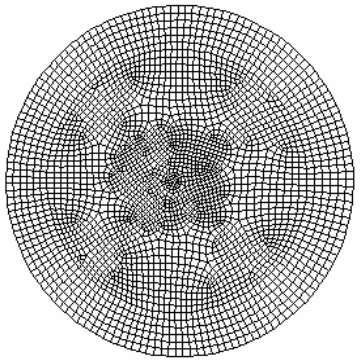

Fig. 3 Grid arrangement along the midsection of the CWBVC chamber.

As usual, the grid is generated in GAMBIT.[7] To decrease the computational time, a Hex mesh is used wherever possible. To produce the Hex mesh, the total volume is decomposed into several parts and the mesh is generated separately for each volume. Figure 2 displays the resulting mesh along the chamber's outer surface. The geometric mesh along the chamber midsection is shown in Fig. 3. This resolution is reproduced identically in the axial direction using the Copper mesh scheme; this particular type sweeps the mesh node patterns of specified source faces through the volume.

Following a grid sensitivity study with successive refinements, the final mesh adopted here comprises an approximate number of 161,084 nodes.

To examine the mesh quality, we refer to the quality-type specification, equiangle skew (Q_{EAS}); this parameter is a normalized measure of skewness and is defined as

$$Q_{\mathrm{EAS}} = \max\left(\frac{\theta_{\max}-\theta_{\mathrm{eq}}}{180-\theta_{\mathrm{eq}}}, \frac{\theta_{\mathrm{eq}}-\theta_{\min}}{\theta_{\mathrm{eq}}}\right) \qquad (1)$$

Here $\theta_{\max}$ and $\theta_{\min}$ are the maximum and minimum angles (in degrees) between the edges of the element, and θ_{eq} is the characteristic angle corresponding to an equilateral cell of similar form. For triangular and tetrahedral elements, $\theta_{\mathrm{eq}} = 60^{\circ}$. For quadrilateral and hexahedral elements, $\theta_{\mathrm{eq}} = 90^{\circ}$. Generally, the mesh will be perfect if $Q_{\mathrm{EAS}} = 0$ and excellent whenever $Q_{\mathrm{EAS}} \le 0.5$. In this study, 99.5% of the cells exhibit a value smaller than 0.5. In fact, the average Q_{EAS} is approximately 0.2, suggesting a mesh of favorable quality.

B. Solver Parameters and Boundary Conditions

The CFD code (FLUENT) is used to solve the steady-state, three-dimensional, Navier-Stokes equations. Within FLUENT, the 3D, segregated, implicit, absolute scheme is utilized. Furthermore, the realizable $\kappa - \varepsilon$ turbulence model of Launder and Spalding[8] is called upon. Reaction mechanisms are simulated using the non-premixed combustion model with the adiabatic PDF look-up tables. The discretization scheme used is PRESTO! (PREssure Staggering Option) for pressure,[7] namely, because the flow is swirl-dominated, and, hence, subject to high-pressure gradients and formidable body forces. The popular SIMPLE pressure-velocity-coupling scheme of Patankar[9] is selected. The discretization schemes for other parameters are set to first-order upwind. Once convergence is achieved by using these discretization schemes, they are changed into second-order upwind schemes for better accuracy. Eight chemical species are involved and, therefore, permitted in the attendant chemical reactions. These include: $O_2, H_2, H_2O, HO_2, H_2O_2, O, H$ and OH.[10] The convergence criterion we adopt is based on a tolerance that ensures that the residual error remains smaller than 10^{-4}. To accelerate convergence and stabilize the iterative process, relaxation factors are, at first, reduced from their aggressive default values. When convergence is approached, relaxation factors are increased to more reasonable values and iterated until convergence is finally achieved.

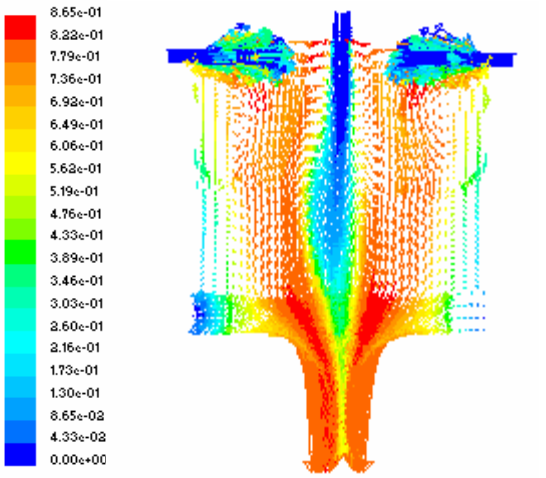

Fig. 4 Predicted velocity vectors along a planar CWBVC cut. Since vectors are colored according to H_2O mass fraction, higher tones represent regions of increasing product concentration.

As for the boundary conditions, nine velocity inlets and one outflow are defined with default interiors and walls. Five velocity inlets are set for GO_2 with an injection speed of 393 ft/sec; these include four tangential inlets at the bottom and one axial inlet at the top. The turbulent intensity and hydraulic diameter are set at 4.73% and 0.111 inch, respectively. Four velocity inlets are defined for GH_2 as it enters the chamber at 1,564 ft/sec in the negative radial direction. The turbulent intensity and hydraulic diameter are set at 5.05% and 0.102 inch, respectively. According to the experimental data and the data used for generating the PDF table, the operating pressure is set at 150 psi at the reference location $(0, 0, 1)$. Following initialization, the code is executed on a P4 Pentium with a 3.0 GHz clock and 3GB of available 400 MHz RAM. After 3,298 iterations, the solution converges using the second-order upwind scheme.

C. Computational Results and Validation

Figures 4 to 9 illustrate the flow characteristics inside the combustion chamber. From the direction of

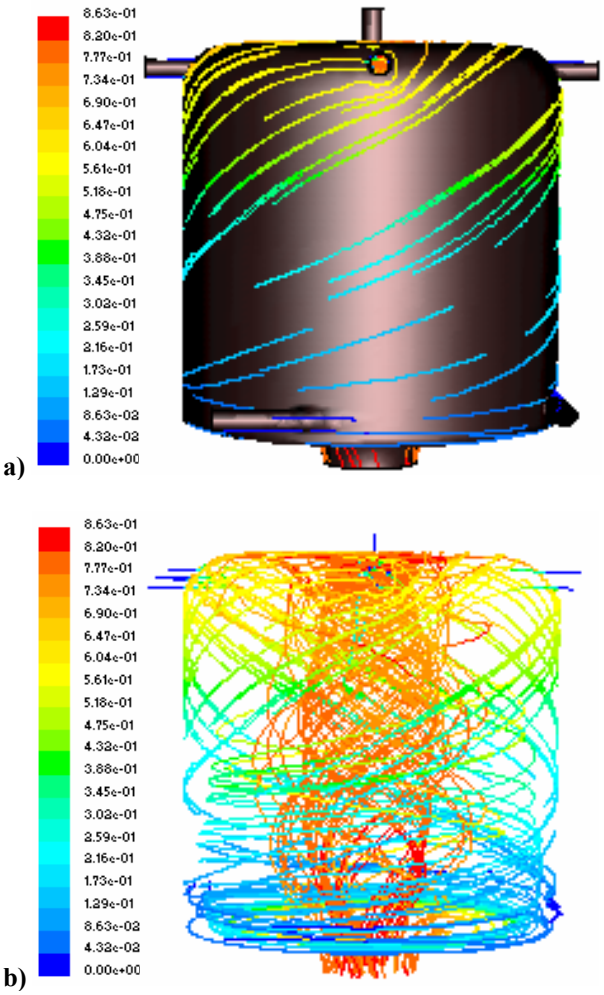

Fig. 5 Display of the pathlines; a) along the chamber wall, and b) across the chamber interior where vectors are colored according to H_2O mass fraction.

the velocity vectors shown in Fig. 4, it can be seen that flow turning occurs near the head end. This confirms the behavior observed experimentally.[3]

Typical flow pathlines that track the motion of the flow are shown in Fig. 5. From Figs. 5a and 5b, we can observe an outer vortex spiraling toward the head end and an inner vortex spiraling toward the nozzle. The flow turning at the head end can also be observed. It should be noted that the pitch of the pathline shown in Fig. 5 changes across the chamber length. It is very small near the end walls and largest halfway across the chamber. This result is gratifying because it confirms the increase in swirl intensity near the end walls where fuel is injected. From a practical standpoint, it justifies the placement of fuel injection near the head end where mixing due to swirl is maximized. In fact, this numerical finding lends support to the conclusion reached in the theoretical study by Vyas, Majdalani and Chiaverini;[4] according to their analytical solution for the mean flow, the swirl intensity is expected to be the largest near the head end.

Details of the velocity character may be extrapolated from Fig. 6 where the axial, tangential, and radial velocity profiles are plotted at four equally spaced axial stations; profiles are located at ratios of $\frac{1}{4}, \frac{2}{4}, \frac{3}{4}$ and 1 of the chamber length measured from the base rather than the head end. At the head end, note that all three components of the velocity vanish, as they should, in fulfillment of the no slip and no flow penetration boundary conditions.

Figure 6a confirms that the axial velocity vanishes not only at the sidewall, but also at an internal node where the flow switches polarity. The location of this internal point coincides with the position of the so-called "mantle" separating the inner vortex from the outer vortex. The latter occupies the annular region in which the primary oxidizer stream spirals around and up the wall.[4-6]

It should also be noted that near the core of the chamber the total velocity is largest in magnitude. Because of the negative axial velocity injection from the top, the flow changes direction near the core, giving the spurious indication that multiple mantles are present.

By analogy with unidirectional flow studies involving swirling motions, one may anticipate a forced vortex in the core region where viscous effects become appreciable. This is confirmed in Fig. 6b which displays features that one may attribute to a forced vortex in the core region, and a free vortex in the outer region. Specifically, one may note the attenuation of the swirl velocity as one approaches the centerline. This result is in qualitative agreement with the explicit formulation obtained by Vyas, Majdalani and Chiaverini[5] where the forced vortex behavior is described. It is also interesting to note that the tangential velocity profile does not change significantly as one crosses from $\frac{1}{4}$ to $\frac{3}{4}$ of the chamber length. This behavior also confirms the widely used assumption of an axially independent swirl velocity away from the end walls. Such an assumption is actually necessary in deriving the analytical solution of the companion papers.[4-6]

Figure 6c displays a characteristic plot of the radial velocity component. The profiles are distorted due to turbulence and asymmetries in mesh discretization. Specifically, the profile is negative from 0.7 to 1 everywhere except along the sidewall where forced vortex motion prevails. The negative radial velocity demonstrates that flow is always crossing from the outer, annular region to the inner, core vortex; it is instrumental in keeping the wall thermally shielded during combustion. The radial change in direction of

the velocity is also effective in mixing the fuel and oxidizer which, in itself, is capable of promoting more efficient combustion. The presence of both positive and negative radial velocities (depending on the axial and radial location in the chamber) suggests the presence of toroidal recirculation zone(s) somewhere near the core. This constitutes an interesting result because of similar recirculation patterns that have been reported in cold-flow vortex chambers. Recently, Anderson *et al*.[11,12] saw evidence of this phenomenon in PIV cold-flow experiments; these were manifested by the presence of particle deposits on the faceplate. Such results are also corroborated through work discussed by Lewellen.[13,14]

In Fig. 6d, the absolute pressure is displayed. The relative small change in pressure beyond the operating value of 150 psi is due to the small chamber diameter (of 2 inches only) and the effect of chemical combustion and mixing which tend to promote a rather constant chamber pressure throughout the chamber. The pressure change is largest near the base and smallest near the head end where combustion takes place.

In Fig. 6e, the mantle location is plotted along the chamber length; it is shown to slightly deviate away from core in the direction of the sidewall as the head end is approached. By limiting our attention to the segment extending from $\frac{1}{4}$ to $\frac{3}{4}$ of the total length, we calculate a mantle location between 0.751 and 0.824 with an average value of 0.789 and a standard deviation of 0.023. This average increases to 0.797 when only the head-end quarter of the chamber is excluded. Considering the three dimensional injection of oxidizer and fuel that takes place near the head end, the location may be considered to be weakly sensitive to the distance along the chamber length. This result is in agreement with Smith[15] whose mantle measurements also appear to be weakly sensitive to the axial distance.

Along the entire chamber length, it may be surprising that, despite endwall effects and both endwall and sidewall injection, the average mantle location is only increased to 0.806 with a median of 0.805 and a standard deviation of 0.058. These results remain in fair agreement with the cold flow mantle prediction of 0.74 obtained previously using an incompressible flow simulation;[1] it may also be compared to the average value of 0.72 obtained experimentally by Smith[15] in his cylindrical (nonreactive) gas cyclone with flat base. It is interesting that the minimum recorded position is 0.708, which nearly approximates the theoretically derived value of $1/\sqrt{2}$ obtained by Vyas, Majdalani and Chiaverini.[4] Despite the presence of intense chemical reactions in the current simulation, it may be interesting to note that the overall gas motion is not significantly

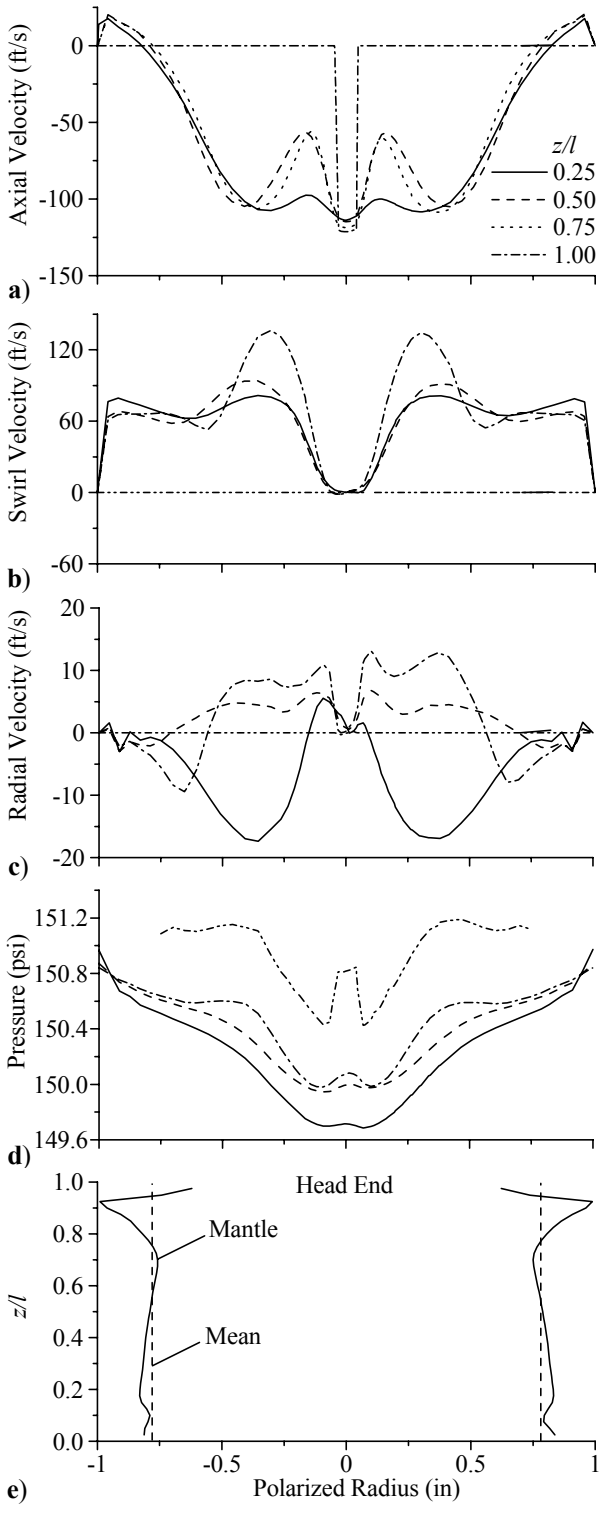

Fig. 6 Planar plot of a) axial, b) radial, c) tangential velocity and d) pressure distributions along the chamber radius. Also shown in e) is the radial movement of the mantle location with the axial distance measured from the CWBVC nozzle base.

altered; the flow characteristics in Fig. 6 compare rather favorably with the cold flow results of Fig. 5 in Ref. 1.

Figure 7 reports the PDF mean mixture fraction parameterized by using a beta-PDF. The PDF is the mixture fraction defined as the mass fraction of fuel in both burned and un-burned forms, and it is described in terms of two parameters: the mixture fraction and the square of fluctuations of mixture fraction (or square of variance of mixture fraction). From the figure we can observe that the elemental mass fraction of fuel is higher near the core and lower near the wall. Near the centerline, the elemental mass fraction of fuel has a small value because of secondary GO_2 injection.

Figure 8 displays the static temperature distribution inside the chamber. It should be noted that the higher temperatures are confined to the core region of the combustion chamber; conversely, the temperatures near the wall are relatively low. The lowered wall temperature is caused by the cooling effect of the outer vortex which carries a chilled fluid. The lowest temperatures are observed near the base and the head end where the cool oxidizer and fuel are injected. The wall temperature has an average temperature of 1,810 K; it varies from 366 K to 2,420 K, with the maximum occurring near $z/l = 0.875$, right below the fuel injection port. The stagnation temperature obtained by CFD is approximately 3,400 K; it is in fair agreement with the theoretically calculated value of 3,300 K; the latter is obtained from a one-step global chemical reaction (see Appendix A). A similar agreement is also obtained in relation to the mass-weighed mean outlet temperature. At the nozzle throat, a CFD prediction of 3,003 K is obtained versus a value of 3,130 K estimated from compressible flow theory (see Appendix B).

Based on Fig. 8, the region near the faceplate appears to be the most susceptible to heating. By way of compensation, design recommendations that may be suggested involve reorienting the fuel and secondary oxidizer injectors to cover more effectively the head-end corners.

Figure 9 displays the species distribution inside the combustion chamber. As shown in Fig. 9a, the mass fraction of O_2 is largest near the wall. The attendant updraft protects the wall from overheating. Conversely, the mass fraction of H_2 shown in Fig. 9b is highest near the head end. This observation justifies the use by Orbital Technologies Corporation (ORBITEC) of a secondary oxygen inlet at the center of the head end to protect the faceplate from thermal loading. As one may infer from Fig. 8, the presence of secondary oxygen injection is required to blow the hydrogen-rich reactants away from the head-end wall. The unburned oxygen in Fig. 9a can be attributed to the high velocity at which the secondary GO_2 is injected from the top. Conversely,

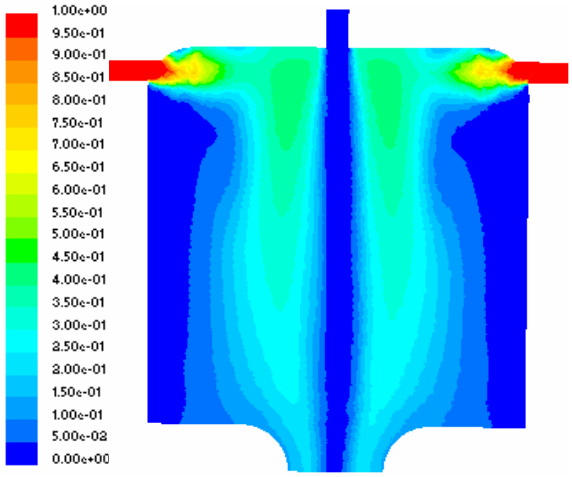

Fig. 7 Display of the normalized mixture fraction.

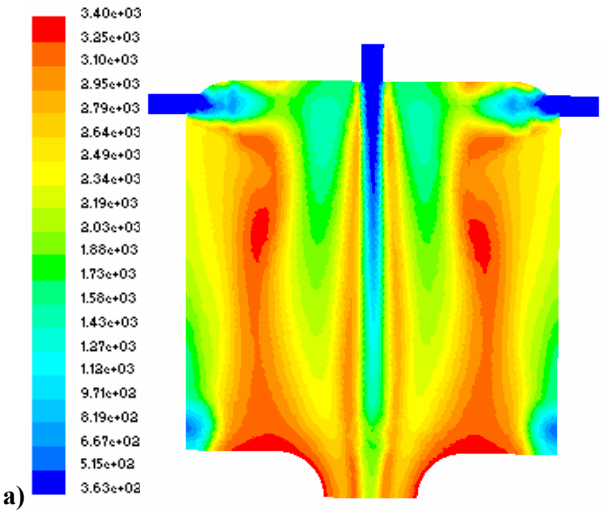

a)

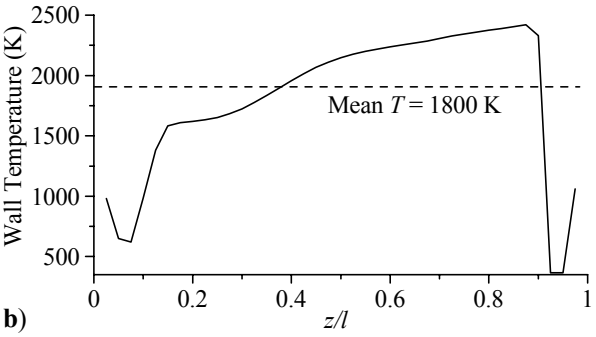

b)

Fig. 8 Maximum temperature distribution a) throughout the chamber and b) along the sidewall assuming adiabatic boundaries.

one may infer from the lower section of Fig. 9b that traces of unburned hydrogen do accompany the flue gases. This observation is consistent with the use of a fuel rich combustion, especially when the equivalence

ratio is 1.33 and the mixture ratio is 6. The presence of unburned hydrogen can also be attributed to the high fuel and oxidizer speed at the injection ports (the inlet velocity of H_2 is about 477 m/s and that of O_2 is about 120 m/s) as well as the low temperature of the injectants (to be conservative, we use 363 K for GO_2 and 366 K for GH_2 in lieu of the boiling temperatures of 90.2 K for GO_2 and 20.3 K for GH_2). From Fig. 9c, one observes a high concentration of water vapor confined near the core; this explains, in part, why the temperature near the wall remains low in comparison to the core. Only traces of hot water vapor are visible near the wall.

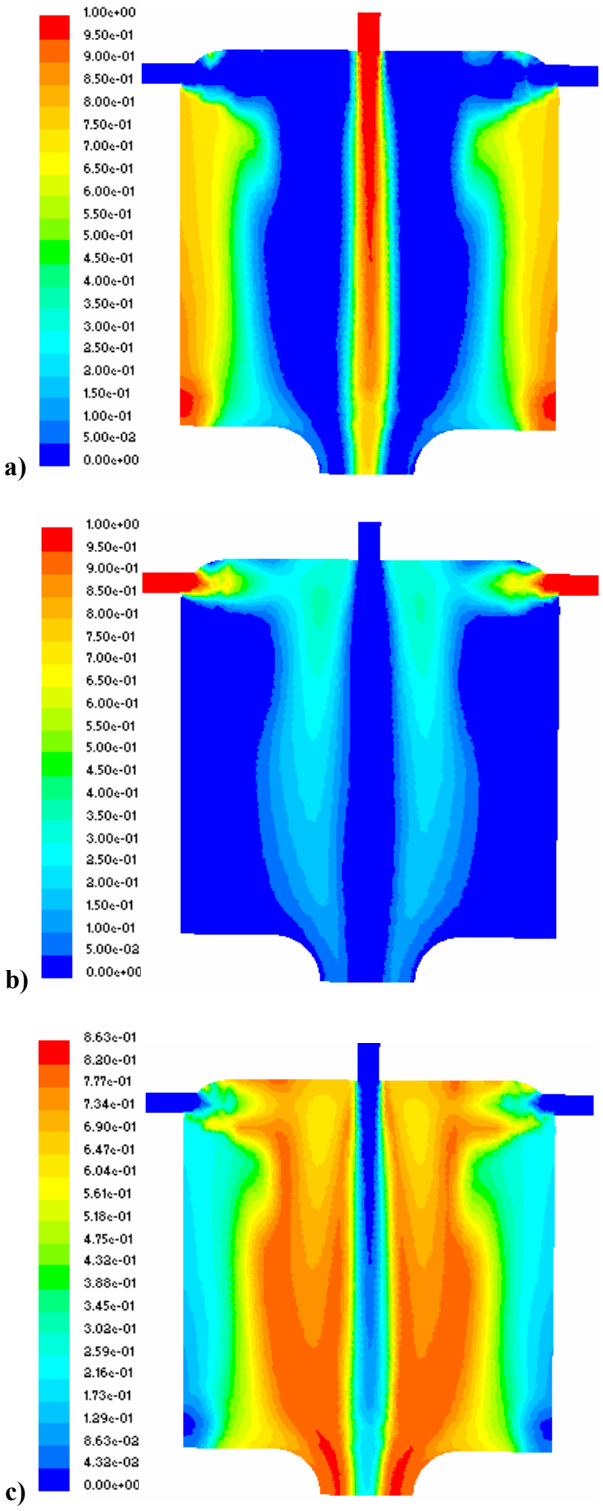

Fig. 9 Predicted species distribution inside the combustion chamber for a) O_2, b) H_2, and c) H_2O.

III. Choked Nozzle Stage II Modeling

A. Computational Domain and Mesh Parameters

During Stage II, the flow is modeled as compressible flow. To capture the compressibility effects, a 'big' computational domain, namely, one which is 15 times larger in each dimension than the object being modeled, is carefully constructed. The computational domain extends well beyond the nozzle itself, so that the domain boundary will not influence the problem unrealistically.

To decrease the computational effort, we assume axisymmetry so that only half of the geometric shape is needed. The essentially two-dimensional geometric mesh is created using GAMBIT and the corresponding computational domain is shown in Fig. 10 after mirroring the view about the centerline of the nozzle. The grid is packed near the wall to help in resolving the turbulent boundary layers. A high grid density is also used near the nozzle exit plane to capture local shocks and expansion waves.

B. Solver Parameters and Boundary Conditions

The coupled, implicit, axisymmetric, steady, absolute solver is chosen to solve the problem. The 'material' associated with the pressure-far-field

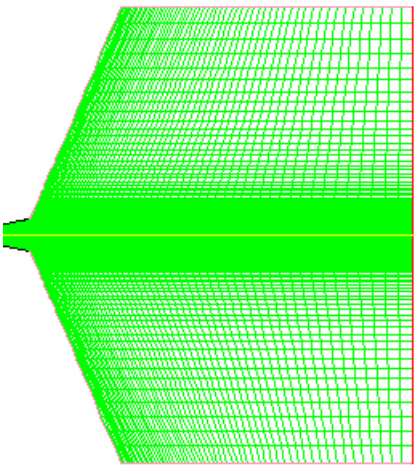

Fig. 10 Computational domain during Stage II used to capture compressibility effects.

boundary condition is defined as an ideal gas. Due to the high Reynolds number and the large pressure gradient inside the nozzle, the RNG $\kappa - \varepsilon$ turbulence model is used with the non-equilibrium wall function treatment to enhance the prediction of the wall shear and the corresponding heat transfer.

Four boundary conditions are employed: one pressure-inlet, one pressure-outlet, and one pressure-far-field with the default wall and interior. To define the boundary conditions, information from the output of Stage I is gathered. Here we assume complete combustion inside the vortex combustion chamber; accordingly, all reactants convert into H_2O. The output from Stage I is summarized in Table 1.

For compressible flow calculations, the parameter of importance is the absolute pressure. For this simulation, the convergence tolerance is set at 0.001. To solve the problem, the first-order scheme is applied and its output used as an initial guess for the second-order solution. The problem is hence initialized and, after 1,556 iterations, the problem converges at the first-order discretization. It requires 1,045 more iterations to reach convergence with the second-order scheme; but even at that time, the mass flow rate does not reach a constant value. To remedy this, we reduce the convergence criterion for continuity down to 0.0001. At the outset, the solution converges after 1,245 more iterations at which time the mass flow rate reaches a constant value as required by global mass conservation.

C. Computational Results and validation

The filled contours of static pressure distributions, Mach number, and temperature are shown in Figs. 11a, b and c, respectively.

From Fig. 11a, one may find that the static pressure contours decrease from the total value to a value lower than the ambient static condition. The pressure will continue to decrease until an oblique shock adjusts the pressure back to the ambient value. However, the flow after the shock will no longer be parallel to the axis. To deflect the flow back, another oblique shock is generated. The nozzle is operated at over-expanded

Table 1 Output from Stage I and input for Stage II

PAR.	DEFINITION	VALUE	UNITS
T	average static temperature	3,003.4	K
P	average static pressure	128.5	psi
κ	average turbulent kinetic energy	4,745.2	m^2/s^2
ε	average turbulent dissipation rate	1.9×10^{-8}	m^2/s^3
m	average mass flow rate	0.086	lbm/s
v	average velocity	2,101	m/s
σ	molecular viscosity	1.7×10^{-5}	kg/(m·s)
c_p	specific heat	3,954	J/(kg·K)
M	mean molecular weight	12.16	-

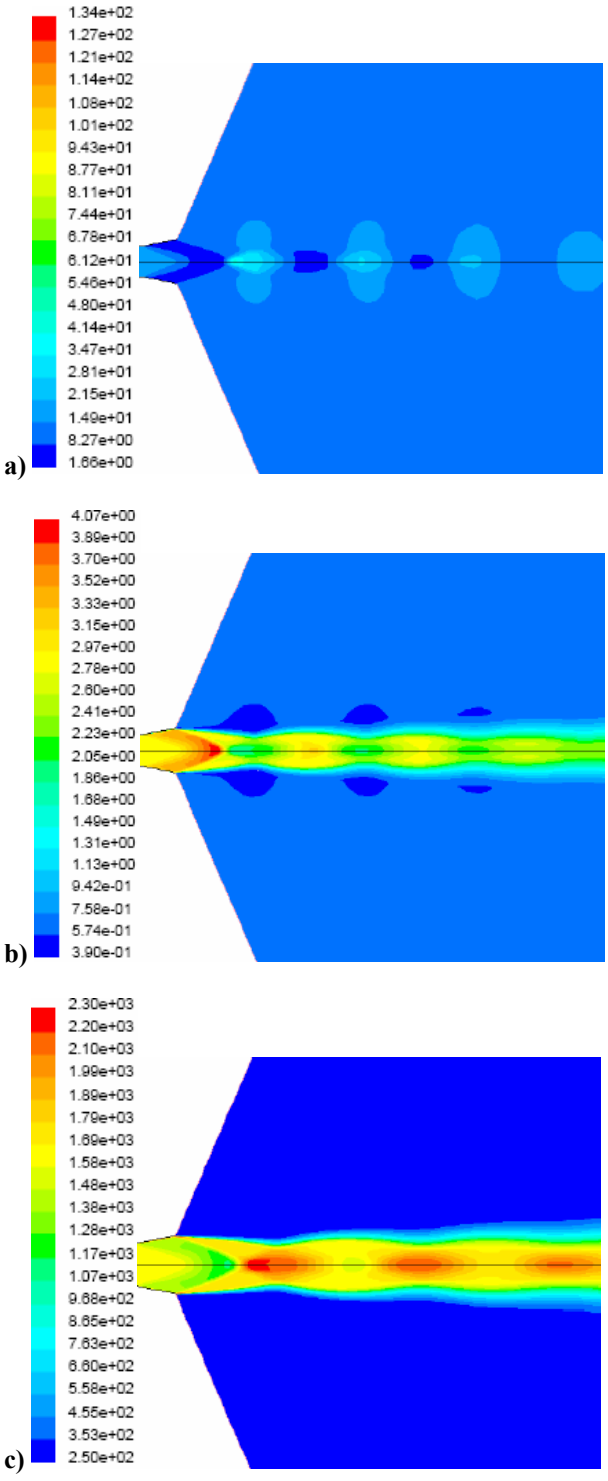

Fig. 11 Contour plots for a) static pressure, b) Mach number, and c) static temperature.

conditions (i.e. the nozzle exit pressure is less than the ambient pressure). One may notice that several oblique shocks are generated downstream of the nozzle exit; as shown in Fig. 11b, the Mach number drops sharply after each shock. The temperature contours in Fig. 11c illustrate the static temperature drop downstream of the nozzle throat along with sporadic temperature jumps where shock waves are formed.

Figure 12 displays the stagnation temperature along the nozzle wall and both static pressure and temperature along the nozzle axis. Along the nozzle centerline the static temperature is observed to decrease at a sharp rate downstream of the nozzle throat; subsequently, several spikes are noted, specifically, at the location of shock waves; these results confirm that, across a shock wave, the static temperature increases abruptly. The centerline pressure downstream of the nozzle exhibits similar trends. As one would expect, the sharp drop in wall stagnation temperature occurs in the nozzle exit plane. After exiting the chamber, 5 shocks are captured in our simulated far field.

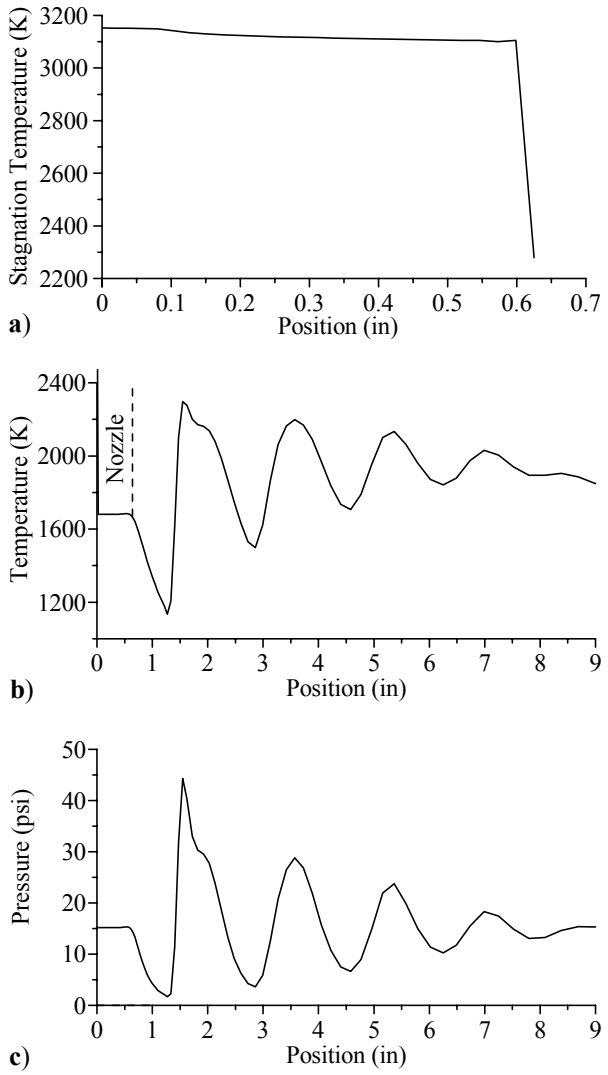

Fig. 12 Planar plots for a) stagnation temperature along the nozzle wall (with a length of 0.625 inch) and both b) static temperature and c) pressure along the nozzle axis (including the pressure far field boundary).

D. Engine Performance

Pursuant to the compressible flow simulation, one can employ the surface integral capability in the CFD code to calculate or recheck the values for:

1. Mass flow rate, $\dot{m}$: 0.0394 kg/s (0.08686 lb/s)
2. Mass-averaged velocity in the exit plane, V_{exit} : 3,573.854 m/s
3. Density in the exit plane, ρ_{exit} : 0.04849 kg/m^3
4. Exit pressure, p_{exit} : 4,9475.55 Pa
5. Ambient pressure, p_{ambient} : 101,185.7 Pa
6. Nozzle outlet area, A_{exit} : 0.0002537 m^2

Based on these numbers, the thrust F produced by the 2×2 CWBVC engine can be estimated from

$$F = \dot{m}V_{\text{exit}} + (p_{\text{exit}} - p_{\text{ambient}})A_{\text{exit}} \tag{2}$$

Readily, one obtains

$$F = 0.03940 \times 3,574 + (49,476 - 101,186) \times 0.0002537$$

$$= 140.8 - 13.12 = 127.7 \text{ N} = 28.7 \text{ lb} \tag{3}$$

The numerically simulated thrust of 28.7 lb falls within 5% of the measured value of (35×0.08686/0.111) = 27.4 lb reported in the live experimental tests conducted by Chiaverini *et al.*[2,3]

Based on Eq. (2), one may deduce the specific impulse; one finds

$$I_{\text{sp}} = \frac{F}{\dot{m}g} = \frac{127.7}{0.03940 \times 9.81} = 330.4 \text{ s} \tag{4}$$

The specific impulse of 330.4 sec is also in agreement with the actual performance value.

IV. Concluding Remarks

In this study, a two-stage numerical simulation is used as a tool for investigating the compressible and reactive field inside the CWBVC. Our simulation suggests that, despite the impact of chemical reactions and their attendant interactions and heat release, the salient features of the bidirectional vortex examined previously under incompressible flow conditions remain valid here. For example, along the segment extending from $\frac{1}{4}$ to $\frac{3}{4}$ of the chamber length, the mantle location is seen to vary between 0.751 and 0.824; the mean value of 0.789 remains in general

agreement with the analytically predicted value of 0.707 rendered from inviscid, nonreactive flow theory. It also compares favorably with the value of 0.74 obtained using an incompressible, reactive flow simulation with no nozzle attachment. When the over-expanded nozzle is accounted for, oblique shock waves are formed. These lead to surges in the static temperatures and pressures.

Also observed here is the forced vortex behavior displayed by the tangential velocity. Such behavior is reported near the core in previous studies using numerical, theoretical and experimental tools.[2,3] The reactive compressible simulation confirms the need to utilize secondary oxygen injection from the top to reduce thermal loading on the faceplate. Presently, the head-end corners appear to be the most susceptible to heating (in addition to the nozzle entrance region). The rest of the chamber displays much lower temperatures. Specifically, the steady-state temperature at the sidewall is shown to yield 1,800 K on average. This result corresponds to an approximate 1,600 K drop in temperature within a one inch radius.

From a heat transfer point of view, this sharp thermal gradient may be deemed spectacular, especially that it corresponds to (a) adiabatic conditions, (b) very short radial distance between combustion products and wall surface, (c) steady, long term operation, and (d) conservative injection temperatures that are much larger than the boiling temperatures of both oxidizer and fuel. In practice, the engine is to be operated for much shorter durations, namely, for seconds or minutes; at the outset, one may clearly argue that, in actual operation, the wall temperature will never attain the conservative steady-state, adiabatic values simulated here. In fact, it may be argued that, despite our plethora of added restrictions, the overall reduction in chamber wall temperature remains quite impressive by any measure; this can be indubitably attributed to the constant presence of cool oxidizer in the annular region separating the combustion products from the wall. Other findings include our observations that:

- The incompressible flow model is adequate everywhere except in the nozzle.
- To model the nozzle properly, a compressible fluid must be used in conjunction with a far field domain surrounding the nozzle.
- The PDF model is suitable for simulating the combustion process.
- The use of a hex mesh can improve the accuracy of CFD predictions and reduce time to convergence.
- The use of adiabatic wall boundary conditions instead of constant heat flux can be helpful in predicting the maximum chamber temperature.

At this juncture, more work is required to estimate important performance parameters such as the torque exerted by the accelerated gases on the nozzle and the thrust/specific impulse for increasing mass flow rate. In future work, we plan to complete a fully compressible and dynamic flow simulation that can capture the temporal evolution of the wall temperature.

Appendix A

The purpose of this appendix is to compare the adiabatic flame temperature (at constant pressure) obtained by CFD to that predicted theoretically.

For the Cold-Wall Vortex Combustion Chamber, the mixture ratio is set at 6. Forthwith, the equivalence ratio can be determined from

$$\phi = \frac{(\mathrm{F/O})}{(\mathrm{F/O})_{\mathrm{st}}} \tag{A1}$$

where the subscript "st" refers to stoichiometric conditions. For hydrogen combustion with pure oxygen the stoichiometric one-step global reaction is, of course,

$$2\mathrm{H}_2 + \mathrm{O}_2 \rightarrow 2\mathrm{H}_2\mathrm{O} \tag{A2}$$

The stoichiometric fuel to air ratio can be determined from the molar contributions viz.

$$\left(\frac{\mathrm{F}}{\mathrm{O}}\right)_{\mathrm{st}} = \frac{2(2.016)}{1(32)} \approx \frac{1}{8} \tag{A3}$$

The equivalence ratio for the CWBVC becomes

$$\phi = \frac{(\mathrm{F/O})}{(\mathrm{F/O})_{\mathrm{st}}} = \frac{1/6}{1/8} = 1.333 \tag{A4}$$

Since $\phi > 1$ a fuel rich condition prevails (as is typical of liquid rocket motor operation). The molar proportion in the CWBVC can be extrapolated from

$$\frac{\mathrm{F}}{\mathrm{O}} = \frac{1}{6} = \frac{x(2.016)}{1(32)} \Rightarrow x = 2.646 \tag{A5}$$

The corresponding one-step global reaction may be written as

$$2.646\mathrm{H}_2 + \mathrm{O}_2 \rightarrow 2\mathrm{H}_2\mathrm{O} + 0.646\mathrm{H}_2 \tag{A6}$$

This reaction implies that, if no intermediate species were to occur, then the water vapor would result only from the stoichiometric combustion of hydrogen and oxygen. As hydrogen is in greater than stoichiometric proportion, it is left uninvolved. The adiabatic flame temperature at constant pressure can now be calculated on the basis of Eq. (A6). Using Turns,[16] one can put

$$H_{\mathrm{reac}}(T_i, P) = H_{\mathrm{prod}}(T_{\mathrm{ad}}, P) \tag{A7}$$

where H is the enthalpy and the subscript 'ad' stands for adiabatic. Equation (A7) can be expressed in further detail by expanding

$$H_{\text{reac}} = \sum_{\text{reac}} N_i h_i, \quad H_{\text{prod}} = \sum_{\text{prod}} N_i h_i \tag{A8}$$

where N_i represents the number of moles (kmol) of the species *i,* and h_i is the total enthalpy associated with a given species. Furthermore, one must recall that

$$h_i = h_{fo,i} + \int_{298}^{T} C_p(T)\mathrm{d}T \tag{A9}$$

where C_p is the specific heat at constant pressure and $h_{fo,i}$ is the enthalpy of formation of species *i* at 298 K.

Because the enthalpy of formation of elements in their naturally occurring states at 298 K is zero, the above equation reduces to terms involving quadrature elements. In the interest of clarity, reactants and products are treated separately in this analysis, albeit standard. First, we begin with the reactants

$$H_{\text{reac}} = \sum_{\text{reac}} N_i h_i = N_{\text{H}_2} h_{\text{H}_2} + N_{\text{O}_2} h_{\text{O}_2}$$

$$= 2.646 h_{\text{H}_2} + h_{\text{O}_2} \tag{A10}$$

where

$$h_{\text{H}_2} = \int_{298}^{300} C_{p,\text{H}_2}(T)\mathrm{d}T; \; h_{\text{O}_2} = \int_{298}^{300} C_{p,\text{O}_2}(T)\mathrm{d}T \tag{A11}$$

The temperature of 300 K for both reactants is chosen for the sake of simplicity. The temperature dependency of the specific heats is culled from Table A.13 in Turns.[16] After simple algebra, one finds

$$H_{\text{reac}} = 211.436 \text{ kJ} \tag{A12}$$

It must be noted that the specific heat variation with temperature is different in the regime up to 1,000 K and between 1,000-5,000 K. For this reason, one can set

$$h_{\text{H}_2\text{O}} = -241845 + \int_{298}^{1000} C_{p,\text{H}_2\text{O}}(T)\mathrm{d}T$$

$$+ \int_{1000}^{T_{ad}} C_{p,\text{H}_2\text{O}}(T)\mathrm{d}T \tag{A13}$$

and

$$h_{\text{H}_2} = \int_{298}^{1000} C_{p,\text{H}_2}(T)\mathrm{d}T + \int_{1000}^{T_{ad}} C_{p,\text{H}_2}(T)\mathrm{d}T \tag{A14}$$

Similary, one can write

$$H_{\text{prod}} = \sum_{\text{prod}} N_i h_i = 2h_{\text{H}_2\text{O}} + 0.646 h_{\text{H}_2} \tag{A15}$$

These lead to

$$H_{\text{prod}} = -489264 + 62.1461 T_{\text{ad}}$$

$$+0.0276253 T_{\text{ad}}^2 - 6.29672 \times 10^{-6} T_{\text{ad}}^3$$

$$+3.72027 \times 10^{-10} T_{\text{ad}}^4 + 4.22899 \times 10^{-13} T_{\text{ad}}^5 \tag{A16}$$

Using Eq. (A7), and solving the polynomial numerically for T_{ad}, one finds

$$T_{\text{ad}} \approx 3{,}300.6 \text{ K} \tag{A17}$$

This result compares favorably with the prediction obtained by CFD.

Appendix B

The purpose of this appendix is to calculate the nozzle throat temperature based on ideal gas behavior. From the input data of Table 1, the chamber pressure is taken to be $p_1 = 150\,\text{psi}$ for a nozzle throat area of $A_t = 0.196\,\text{in}^2$. Because the nozzle is choked, the Mach number at the throat is unity, i.e. $M_t = 1$.

By assuming complete combustion we utilize the specific heat ratio for water vapor, namely $k = 1.3$. Using standard notation and ideal gas behavior, the throat-to-chamber pressure ratio can be estimated from

$$\frac{p_t}{p_1} = \left[2/(k+1)\right]^{k(k+1)} \tag{B1}$$

The corresponding throat pressure is calculated to be

$$p_t = 150 \times \left[2/(1.3+1)\right]^{1.3\times(1.3+1)} = 142.03 \text{ psi} \tag{B2}$$

Interestingly, this theoretical value is not too dissimilar from the CFD estimate of $p_t = 128$ psi. For an adiabatic flame temperature of $T_1 = 3{,}300$ K, the throat temperature can be readily determined from

$$T_t = 2T_1/(k+1) = 2 \times 3{,}300/(1.3+1) = 2{,}870 \text{ K} \tag{B3}$$

However, using the experimental value of $T_1 = 3{,}600$ K, the throat temperature can be similarly calculated to be $T_t = 3{,}130$ K. Both calculation results fall within 4% of the CFD value of $T_t = 3{,}003$ K.

Acknowledgments

This work was performed according to Orbital Technologies Corporation (ORBITEC) subcontract no. OTC-GS-0122-3A, drawn from prime contract no. NAS8-02020 of a NASA Phase II SBIR project entitled, "Vortex Combustion Cold-Wall Chamber." The support and encouragement of Mr. Richard Cooper and Mr. Huu Trinh, Technical Monitors at NASA Marshall Space Flight Center, are most gratefully acknowledged. The authors are indebted to Dr. Anand B. Vyas for his assistance in conducting this work. We also thank Dr. Mark Anderson and Mr. Craig Rom from the University of Wisconsin, Madison; their input and data exchange are greatly appreciated. Finally, we thank Mr. William H. Knuth and Mr. Ronald R. Teeter of Orbital Technologies Corporation for their insightful comments and suggestions during the course of this investigation.

References

[1]Fang, D., Majdalani, J., and Chiaverini, M. J., "Simulation of the Cold-Wall Swirl Driven Combustion Chamber," AIAA Paper 2003-5055, July 2003.

[2]Chiaverini, M. J., Malecki, M. J., Sauer, J. A., and Knuth, W. H., "Vortex Combustion Chamber Development for Future Liquid Rocket Engine Applications," AIAA Paper 2002-2149, July 2002.

[3]Chiaverini, M. J., Malecki, M. J., Sauer, J. A., Knuth, W. H., and Majdalani, J., "Vortex Thrust Chamber Testing and Analysis for O2-H2 Propulsion Applications," AIAA Paper 2003-4473, July 2003.

[4]Vyas, A. B., Majdalani, J., and Chiaverini, M. J., "The Bidirectional Vortex. Part 1: An Exact Inviscid Solution," AIAA Paper 2003-5052, July 2003.

[5]Vyas, A. B., Majdalani, J., and Chiaverini, M. J., "The Bidirectional Vortex. Part 2: Viscous Core Corrections," AIAA Paper 2003-5053, July 2003.

[6]Vyas, A. B., Majdalani, J., and Chiaverini, M. J., "The Bidirectional Vortex. Part 3: Multiple Solutions," AIAA Paper 2003-5054, July 2003.

[7]*Fluent UNS Theory Manual*, 6.1 ed., Fluent Inc., Palo Alto, California, 2002.

[8]Launder, B. E., and Spalding, D. B., "The Numerical Computation of Turbulent Flows," *Computational Methods in Applied Mechanical Engineering,* Vol. 3, 1974, pp. 369-289.

[9]Patankar, S. V., *Numerical Heat Transfer and Fluid Flow*, Hemisphere, Washington, D.C., 1980.

[10]Peters, N., "Flame Calculations with Reduced Mechanisms: An Outline," *Reduced Kinetic Mechanisms for Applications in Combustion Systems*, edited by N. Peters and B. Rogg, Springer-Verlag, 1993.

[11]Anderson, M., Valenzuela, R., Rom, C., Bonazza, R., and Chiaverini, M. J., "Vortex Chamber Flow Field Characterization for Gelled Propellant Combustor Applications," AIAA Paper 2003-4474, July 2003.

[12]Anderson, M., Rom, C., and Chiaverini, M. J., "Cold Flow Analysis of a Vortex Chamber Engine for Gelled Propellant Combustor Applications," AIAA Paper 2004-3359, July 2004.

[13]Lewellen, W. S., "A Review of Confined Vortex Flows," NASA, Technical Rept. CR-1772, July 1971.

[14]Lewellen, W. S., Burns, W. J., and Strickland, H. J., "Transonic Swirling Flow," *AIAA Journal,* Vol. 7, No. 7, 1969, pp. 1290-1297.

[15]Smith, J. L., "An Analysis of the Vortex Flow in the Cyclone Separator," *Journal of Basic Engineering-Transactions of the ASME*, 1962, pp. 609-618.

[16]Turns, S. R., *An Introduction to Combustion: Concepts and Applications*, 2nd ed., McGraw-Hill, New York, 1996.